ECS | The Electrochemical Society
Advancing solid state & electrochemical science & technology

Effects of Distribution Zone Design on Flow Uniformity and Pressure Drop in PEMFC

To cite this article: Yuan Yu *et al* 2021 *J. Electrochem. Soc.* **168** 094505

View the article online for updates and enhancements.

Effects of Distribution Zone Design on Flow Uniformity and Pressure Drop in PEMFC

Yuan Yu,[1,2] Zhigang Zhan,[1,2,3,z] Luyan He,[1,2] Xiaoxiang Yang,[1,2] Xiongbiao Wan,[1,2] Pang-Chieh Sui,[1,3,4,z] and Mu Pan[1,2,3]

[1]Foshan Xianhu Laboratory of the Advanced Energy Science and Technology Guangdong Laboratory, Xianhu hydrogen Valley, Foshan 528200, People's Republic of China
[2]State Key Laboratory of Advanced Technology for Materials Synthesis and Processing, Wuhan University of Technology, Hubei 430070, People's Republic of China
[3]School of Automotive Engineering, Wuhan University of Technology, Hubei 430070, People's Republic of China
[4]Institute for Integrated Energy Systems, University of Victoria, Victoria BC, Canada

A typical flow field plate of proton exchange membrane fuel cells has a distribution zone that connects the input ports and main channel region where major reactions take place. In this study, the effects of two distribution zone designs, i.e., the channel-ridge distribution zone (CRDZ) and dot matrix distribution zone (DMDZ), on the gas distribution uniformity and pressure drop are investigated numerically. For the flow fields with CRDZ, the theoretical mass flow rates and pressure distributions are found to agree with numerical results well. The flow rate distributions in the flow fields become more uniform when the turning angle increases to special angle. To design the flow fields with CRDZ, the channels can be arranged with simple geometry lines in the first step and then optimised with CFD considering the actual size to achieve a more uniform distribution and suitable pressure drop. For the flow fields with DMDZ, the uniformity of gas distribution depends on the shunt and dispersion effects of dot matrix, and the rectification and expansion effects of the distribution chamber. With an increase in porosity of DMDZ, the gas distribution gets better, and it is the most uniform when the distribution zone is an empty chamber.

The flow field plates in a proton exchange membrane fuel cell (PEMFC) play an important role in reactants supply, product water removal, electron conduction, heat transfer, and mechanical support.[1] Proper design of these plates would facilitate uniform distribution of reactants over the membrane electrode assembly (MEA), fully utilizing the catalyst layers for electrochemical reactions. An ideal flow field plate should also establish a suitable pressure gradient that is sufficiently high to blow liquid water out of the gas channels, yet low enough to maintain both uniform electrochemical reactions along the gas channels, and a low demand of pumping power.

Several types of conventional flow field design have been developed, such as the parallel, serpentine, interdigitated flow fields.[2–10] New structure designs based on them have also been proposed and studied. Yan et al.[11] investigated five different types of flow field designs including the parallel, the Z-type, the serpentine, the parallel with baffles, and the Z-type with baffles. They found the parallel flow field with baffles was the best design by considering the cell performance together with the pressure drop. Choi et al.[12] investigated the effects of single, double, and mixed serpentine channel flow patterns on the distribution of internal properties in a counter-flow PEMFC under cathode starvation conditions through numerical studies and experiments. Tong et al.[13] tested a parallel flow field design with two external regulation valves, which could create a new flow pattern with a more uniform pressure difference at the land area that induced cross flow along the channel, thus improving the overall cell performance. Parallel flow field design does not incur significant pumping losses or large concentration gradients, which are often encountered in serpentine or interdigitated flow field designs. Guo et al.[14] developed a network-based optimization model considering reactant consumption. Different flow field configurations, including parallel, parallel-in-series, and serpentine designs, were optimized using their model. Mojica et al.[15] experimentally and numerically studied straight parallel, multiple channel serpentine, and single channel serpentine flow field designs, and concluded that the multiple channel serpentine design can provide a

reasonable balance between pressure drop and flow distribution with robust fuel cell operation. Atyabi et al.[16] examined a sinusoidal flow field and compared it with a straight-parallel configuration using a non-isothermal, steady-state, and multiphase model. Their results showed that the sinusoidal flow field achieved better performance than the straight-parallel flow field. Chowdhury et al.[17,18] studied convergent/divergent serpentine and parallel-flow fields using numerical and experimental methods. The channel depth was varied via inclination from the inlet to outlet, which created a convergent/divergent flow effect. Compared with the conventional flow field, the cell performance with this design was significantly better.

To promote oxygen transport and improve distribution uniformity, novel flow field designs have been developed, such as the three-dimensional (3D), bionic flow fields. Toyota reported a 3D flow field design[19] used in the stack of their Mirai fuel cell vehicle. This design enhanced oxygen transport towards the cathode catalyst layer and improved the discharge of liquid water. Kim et al.[20] attempted to reveal the enhanced mass transport mechanism in 3D flow fields, while Zhang et al.[21] and Li et al.[22] attempted new 3D structures. Mojica et al.[23] performed a comprehensive study of four flow channel designs: straight, wavy, 2D-Nozzle, and the novel 3D-Nozzle, the result shown that the peak power density of the 3D-Nozzle design is 25% higher than all other designs. Flow field designs based on bionic features have been proposed by a few groups. These bionic structures are a result of natural evolution owing to their advantages in mass transfer. Theoretically, these types of structures are also suitable for delivering a mass with high efficiency.[24] Two types of flow patterns, namely the leaf and the lung designs, were proposed by Kloess et al.[25] A biophysical flow field designed to mimic features of vascular flow networks was used by Wang et al.[26] Tuber et al.[27] developed a computer algorithm to provide a given area with a multiple ramified fluid network by virtue of self-similarity or fractal structure, which were investigated and compared with common serpentine and parallel flow fields for PEMFCs. Fractal flow fields exhibit performances similar to those of parallel designs. Wen et al.[28,29] proposed another fractal structure, i.e., the so-called intersectant flow field. The flow channels in the flow field were at an acute angle, which was decided based on Murray's law. Their experimental results indicated that fuel cells

[z]E-mail: zzg-j@163.com; jsui@uvic.ca

with bionic features performed better than the conventional flow field design under the same operating conditions, mainly because of the uniformity of flow distribution.

Ideally, maximum cell/stack performance at any operating conditions could be obtained when all the fluid flows in the unit cell are evenly distributed, although in reality this goal is almost impossible to be achieved. The gas distribution uniformity among the unit cells in stacks and the uniformity and the pressure drop among the channels in flow fields have been studied by several research groups.[30–33] Among them, Chen et al.[30] numerically investigated the effects of stack structure and size on the gas distribution and pressure variation among the unit cells, while Su et al.[31] studied the effects of vortexes in feed header on air flow distribution of PEMFC stack. For simplicity, they all assumed the air as incompressible ideal gas and ignored electrochemistry, heat and mass transport phenomena. Barreras et al.[32,33] investigated the flow distribution in a bipolar plate of a PEMFC by numerical and experimental methods, where air was replaced by water in order to

visualize the flow pattern. They found the flow distribution among the channels in the bipolar plate was non-uniform. Cai et al.[34] numerically studied a novel 3D cathode flow field and proposed evaluation criteria for the PEM fuel cell design. They concluded that high velocity and low pressure drop result in high criteria and good cell performance. Furthermore, it was found that porous ribs could improve distribution uniformity and performance. Liu et al.[35] studied the relationship between the flow field plate and the pressure drop. The effects of pressure drop on the cost of hydrogen due to the different hydrogen usage efficiency were analyzed and compared for three types of flow field plates. They concluded their novel flow field plate not only lowered the pressure drop but also reduced the composite cost.

Practical flow field plates for automotive applications are in the order of several hundred cm^2.[36,37] The flow field in these plates can be divided into three zones: inlet/outlet, distribution/collection (in most cases they have symmetric structures), and reaction zone. Previous studies have focused mainly on the reaction zone in the flow field. The distribution zone may significantly affect the flow distribution and pressure drop, but
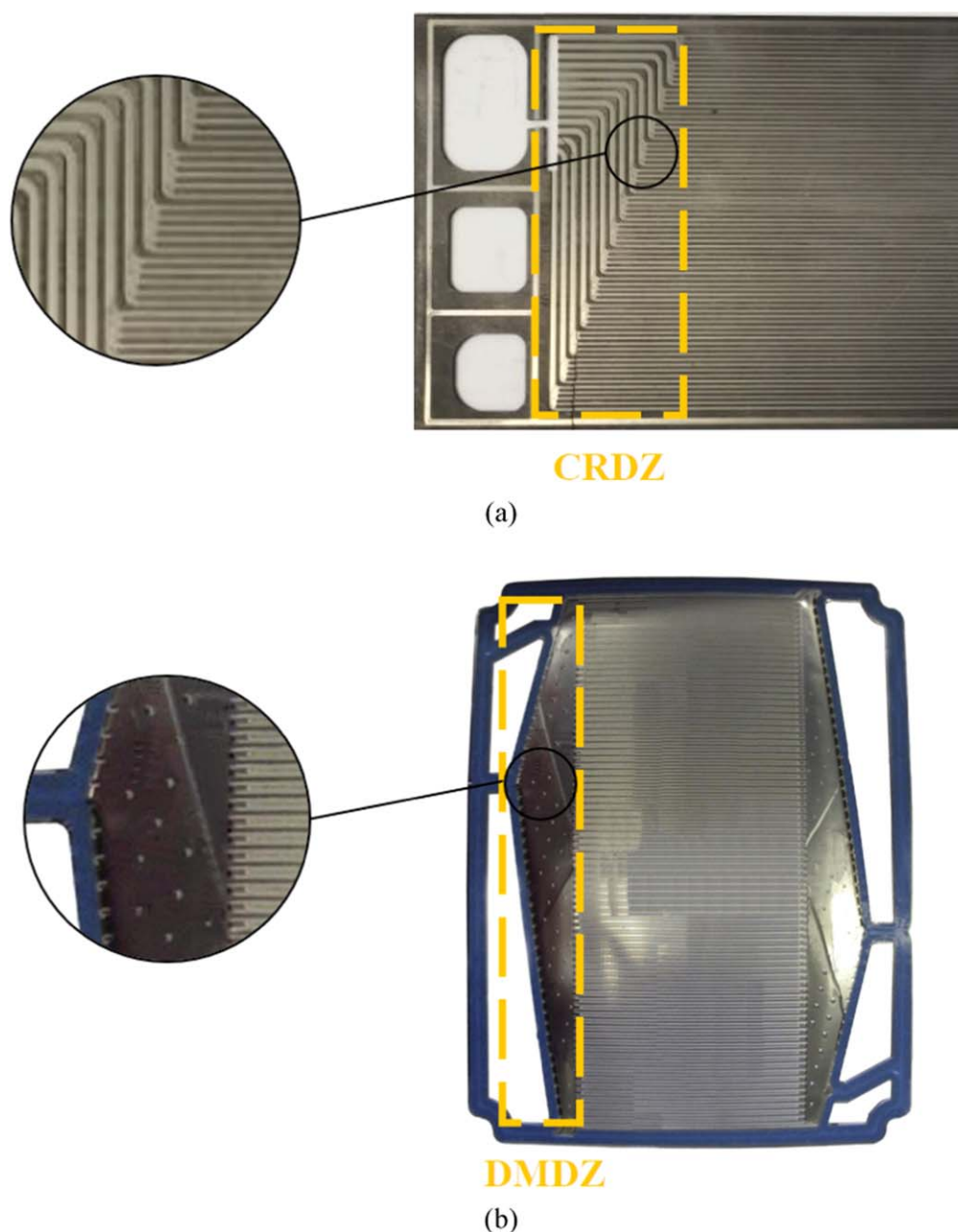

Figure 1. Geometry of flow field plates with (a) CRDZ, (b) DMDZ design (adapted from Ref. 39 with permission).
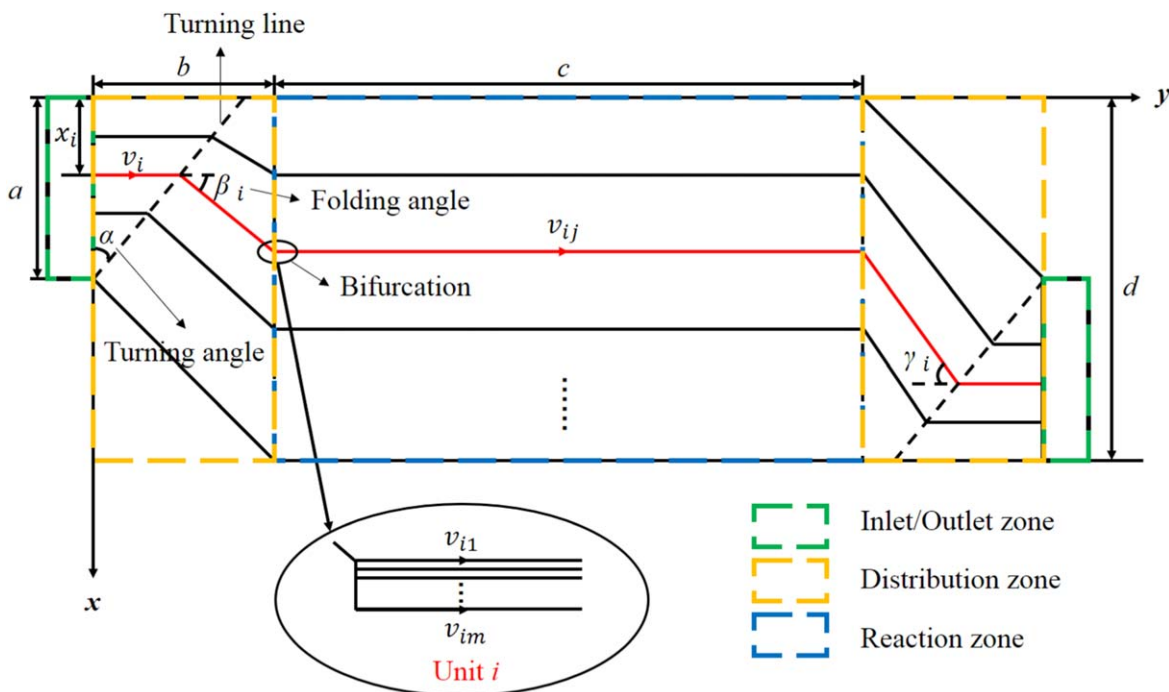
Figure 2. Generalized layout of a channel-ridge flow field plate.

to date only a few studies have been reported. The above review of literature indicates that systematic studies and practical guidelines on how gas uniformity and pressure drop are affected by the distribution zone are lacking. In this study, two types of distribution zone design, i.e., the channel-ridge (CR) type and the dot matrix (DM) type, are investigated. The effects of the CR and DM designs on gas distribution uniformity and pressure drop are analyzed based on theoretical fluid dynamics and the theory of packed bed, respectively. Subsequently, a series of flow field geometries with different types of distribution zones are designed. The impacts of various distribution zone structures are studied using computational fluid dynamics (CFD). Finally, some conclusions that have practical significance for the flow field design are summarized.

Theoretical Analysis

The fluid flow in a PEMFC flow field plate consists of gases, and often time with liquid water. To make the analysis and simulation simple and straightforward, a few assumptions are made in the present study:

(1) Single phase flow, which implies any liquid water exists as a mist well mixed with all gases.[17,38] In reality, liquid water moves rapidly in the gas channels and time-averaged behaviour of water droplets should not affect the uniformity of gas distribution. However, this assumption fails when there is uneven temperature distribution in the unit cell, which would result into uneven rate of water removal from the flow field plate due to local accumulation of liquid water.

(2) Mass flow rate change in the channels due to electrochemical reactions is negligible.[31] This is arguably acceptable for the cathode side because nitrogen gas contributes the major composition of the gas mixture, whereas the oxygen consumed is compensated partially by water vapor produced.

(3) Pressure-drop due to the presence of liquid water as well as roughness of all channel surfaces is not considered in the calculation. The contributions due to water and surface roughness, especially the GDL surface, can be included ad hoc to match experimental data more accurately.

(4) The system is isothermal and reaches a steady state.

In designing the flow field plates for automotive fuel cell stacks, the dimensions of the inlet port and the distribution zone are often made as large as possible in order to achieve uniform reactant gas distribution, especially for cathode flow fields.[37] Figure 1 shows two typical flow field plates with channel-ridge distribution zone (hereafter termed as CRDZ) and dot-matrix distribution zone (DMDZ) patterns, respectively. The former design features flow paths separated by dividers, whereas the latter uses blocks to facilitate flow mixing. In this section, flow distributions of the CRDZ and DMDZ designs are analysed based on theoretical fluid dynamics and the theory of packed bed, respectively.

Channel-ridge distribution zone.—Figure 2 shows a generalized layout of a CRDZ flow field. Fluid flows through the inlet, distribution zone, reaction zone, collection zone and finally the outlet. The design is characterized with dimensions of a, b, c, and d and angles α, β_i and γ_i. The ith flow from the distribution zone at velocity v_i may bifurcate into m channels when entering the reaction zone with velocity v_{ij}, and then merge after leaving the reaction zone. The parameters in Fig. 2 are summarized in Table I.

To investigate how channel arrangement affects flow distribution, each flow channel is assumed to be a polyline in the following analysis, e.g., following the red line marked in Fig. 2. The actual width and depth of the flow channel are not considered in this estimate at first. The reactant gas is assumed laminar in the flow field due to its low Reynolds number.[37] The pressure drop in each channel includes the frictional and local resistance losses, which are:[40]

$$p_f = \lambda \frac{l}{d_e} \times \frac{\rho v^2}{2} = \frac{32\mu l}{d_e^2} v = klv \qquad [1]$$

where p_f is the frictional resistance loss, λ is the frictional resistance coefficient, l is the channel length, d_e is the hydraulic diameter, ρ is the gas density, v is the average flow velocity, μ is the fluid viscosity and $k = \frac{32\mu}{d_e^2}$.

$$p_m = \zeta \frac{\rho v^2}{2} \qquad [2]$$

where p_m is the local resistance loss, ζ is the local resistance coefficient. The total pressure drop is the sum of both losses:
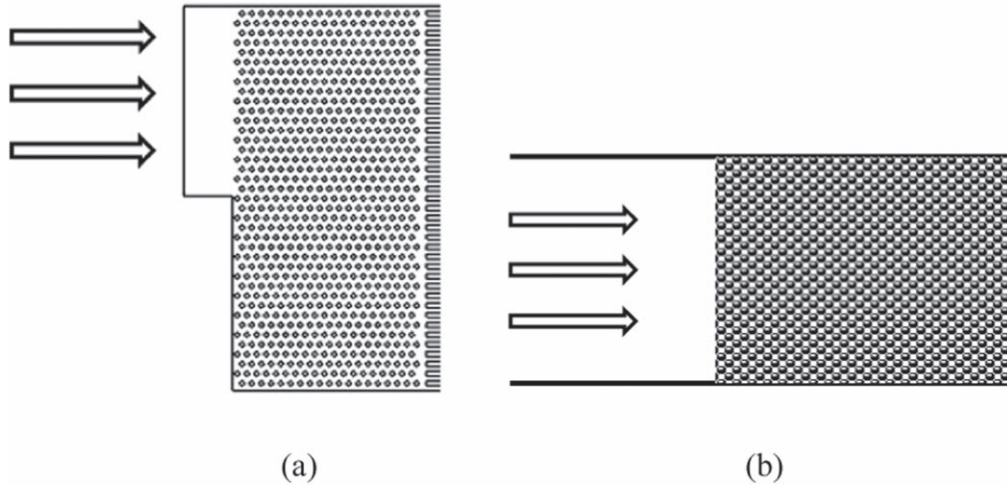
Figure 3. Structures of (a) DMDZ and (b) plane packed bed.

$$p_w = \sum p_f + \sum p_m \qquad [3]$$

Based on the geometric relationships shown in Fig. 2, we have:

$$N = nm \qquad [4]$$

where n and N are the numbers of channels in the distribution and reaction zones, respectively. The gas in the distribution zone is assumed to be evenly distributed to the reaction zone in each unit. The flow velocities in the reaction zone are related to the velocity in the distribution zone as:

$$v_i = mv_{ij} \qquad [5]$$

The distance between the ith channel and the origin can be expressed as:

$$x_i = \frac{i-1}{n-1}a \qquad [6]$$

The relationship between the widths of the inlet and flow field is as:

$$a = \frac{d}{m} \qquad [7]$$

The turning angle is between $0°$ and α_0, where α_0 is a special turning angle, which can be expressed as:

$$\alpha_0 = \arctan\left(\frac{b}{a}\right) \qquad [8]$$

The folding angles, β_i/γ_i, are between β_{i0}/γ_{i0} and $90°$, where β_{i0}/γ_{i0} are the special folding angles, which can be expressed as

$$\tan \beta_{i0} = \frac{(m-1)x_i}{b - (a - x_i)\tan \alpha} \qquad [9]$$

$$\tan \gamma_{i0} = \frac{(m-1)(a - x_i)}{b - x_i \tan \alpha} \qquad [10]$$
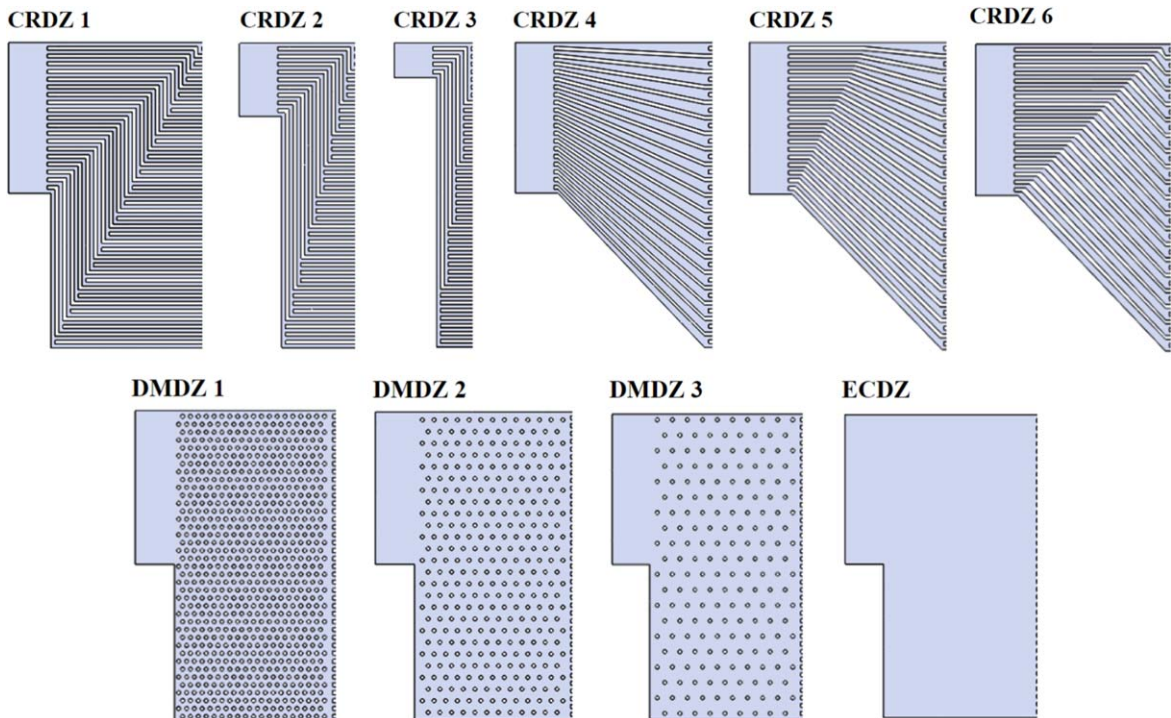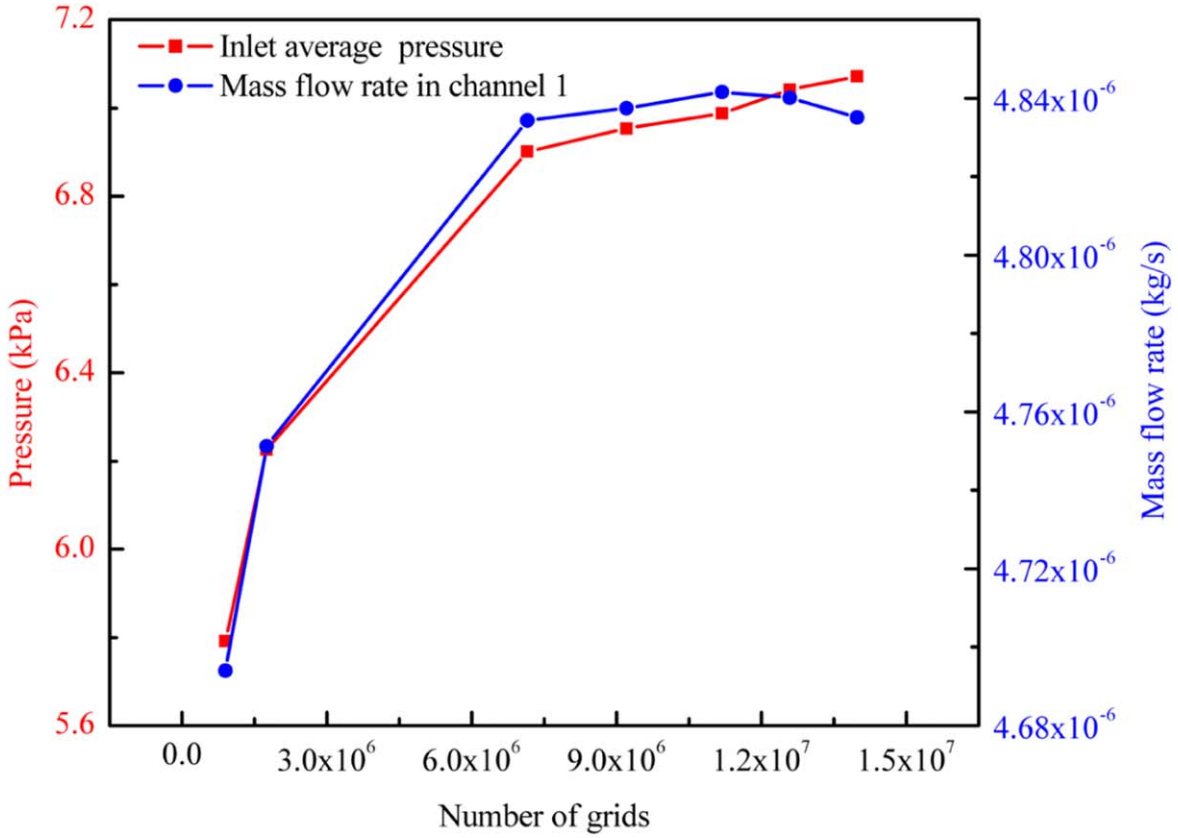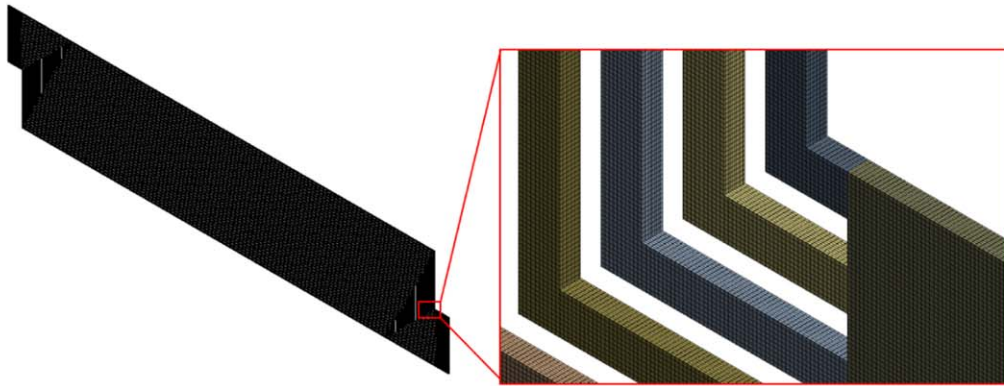

Figure 4. Schematic of the ten distribution zones investigated in the present study.

(a)

(b)

Figure 5. (a) Grid independence test. (b) The grid structure of the flow field with CRDZ 1.

The total mass flow rate can be expressed as:

$$Q = \sum_n^{i=1} Q_i = \sum_n^{i=1} \rho v_i A \qquad [11]$$

where Q_i is the mass flow rate of each channel in the distribution zone, and A is the cross-sectional area of the channel.

The pressure drop in each unit can then be expressed as:

$$p_w(i) = kl_{dis}v_i + kl_{re}v_{ij} + (\zeta_{i1} + \zeta_{i2})\rho v_i^2 = \Delta P \qquad [12]$$

$$\zeta = 0.946 sin^2\left(\frac{\theta}{2}\right) + 2.407 sin^4\left(\frac{\theta}{2}\right) \qquad [13]$$

where l_{dis} and l_{re} are the lengths of the distribution and reaction zone channels, respectively. ζ_{i1} and ζ_{i2} are the two local resistance coefficients related to the folding angles in Unit i.[40]

Thus, the mass flow rate of each channel and the pressure drop in various flow fields with CRDZ can be calculated using Eqs. 11 and 12.

Dot matrix distribution zone.—The DMDZ features a flow field with arrays of blocks in the flow pathway, see Fig. 3a, which
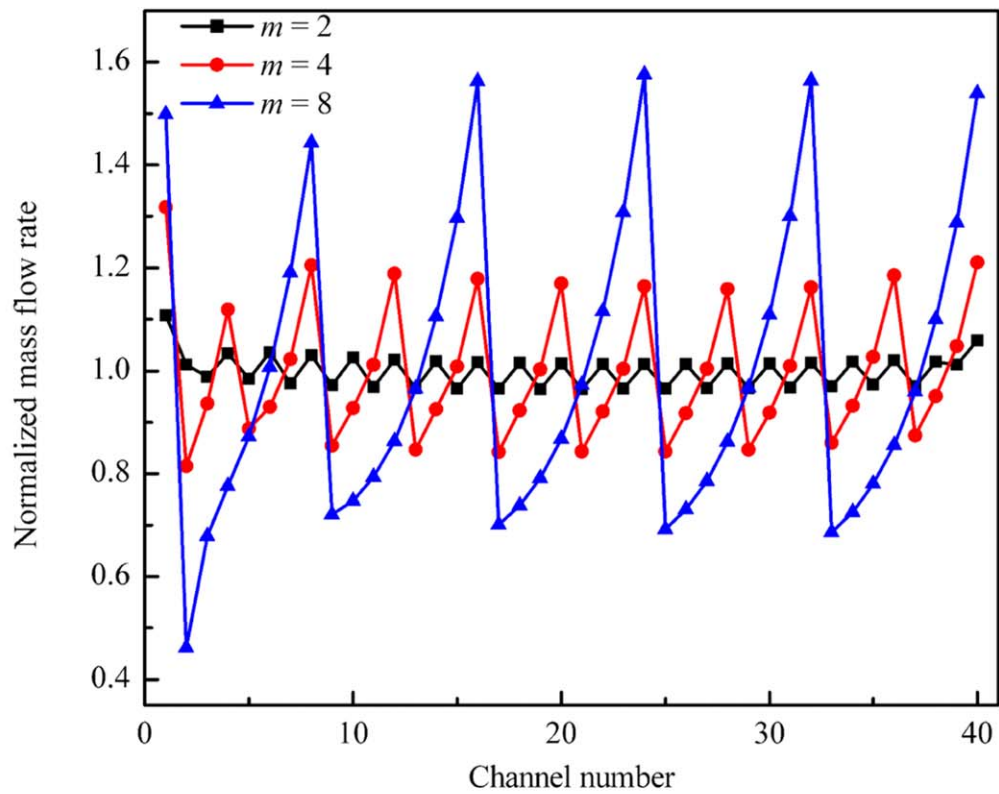
(a)
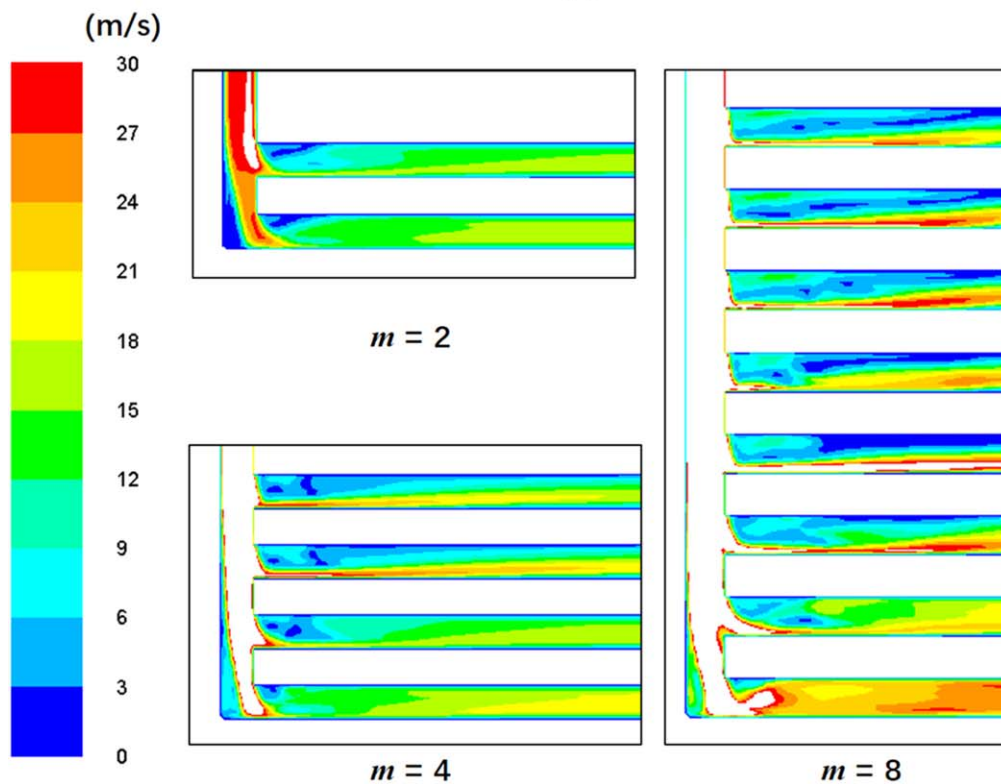
(b)

Figure 6. (a) Normalized mass flow rate distributions in flow fields (the first channel is at the top); (b) Comparison of flow velocities in one unit of flow fields with CRDZ 1–3 at 1.746×10^{-4} kg s^{-1}.
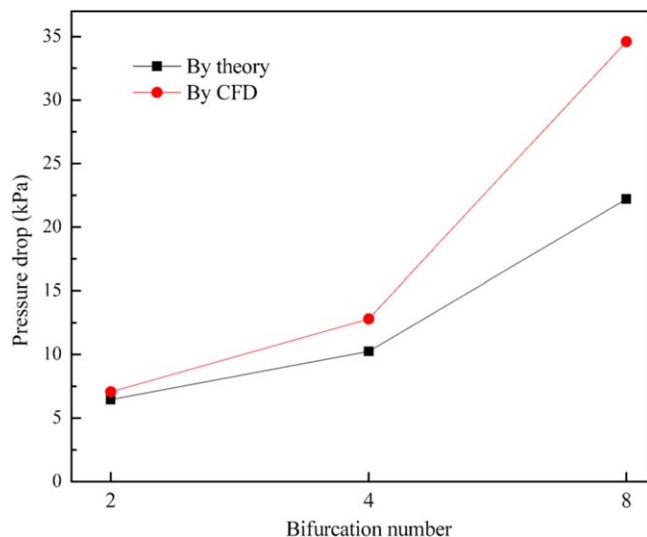
Figure 7. Comparison of pressure drops of flow fields with CRDZ 1–3 at 1.746×10^{-4} kg s^{-1} obtained by theory and CFD.

resembles the flow through a packed bed, see Fig. 3b. The DMDZ can thus be modeled to a plane packed bed, whose uniformity of gas distribution depends on the shunt and dispersion effects of the dot matrix and the rectification and expansion effects of the distribution chamber. Here, the shunt effect is the one that the fluid can be induced to flow in the hoped direction if the dots are arranged highly ordered;[41] the dispersion effect is the one that the fluid can be divided into many branches randomly if the dots are arranged at random;[42] the rectification effect is the one that the fluid must be adjust its flow state according to the flow space shape of the flow channel; the expansion effect is the one that the pressure and speed can be changed into each other according to Bernoulli's equation when the flow section area changed.

The pressure drop of the gas flow through a plane packed bed can be expressed as:[43]

$$\Delta P = \left(150 \times \frac{(1-\varepsilon)^2}{\varepsilon^3} \frac{\mu v}{(\Phi d)^2} + 1.75 \times \frac{1-\varepsilon}{\varepsilon^3} \frac{\rho v^2}{\Phi d}\right) \times l \quad [14]$$

where ΔP is the pressure drop, ε is the porosity, μ is the fluid viscosity, v is the average flow velocity, Φ is the particle shape coefficient, d is the particle diameter, ρ is the gas density, and l is the depth of the field. As shown in Eq. 14, the pressure drop through a packed bed decreases with increasing porosity. To simplify the analysis, the dots are assumed to be cylinders of equal diameter. The gas mixture may be evenly distributed by changing the specific

Table I. Definition of parameters.

Parameters	Definition
a	Width of the inlet zone
b	Length of the distribution zone
c	Length of the reaction zone
d	Width of the flow field
α	Turning angle (the angle between the inlet and turning line)
β_i/γ_i	Folding angles
m	Bifurcation number
i	The ith channel in the distribution zone and m channels in the reaction zone
v_i	Flow velocity in the distribution zone of Unit i
v_{ij}	Flow velocity in the jth channel in the reaction zone of Unit i
x_i	Distance between the ith channel and the origin

shape and orientation arrangement of dots in the distribution zone, i.e., by the shunt effect of dot matrix.

The distribution zone can be regarded as a chamber, and the cross-sectional area of the gas flow usually increases from the inlet of the distribution zone to its outlet, which has the effects of rectification and expansion on the gas flow. With a decrease in the dot size or density of the dot matrix (the number of dots in unit area), the porosity of the distribution zone increases, and the rectification and expansion effects of the chamber enhance, resulting in a more uniform gas distribution. In particular, the DMDZ becomes an empty chamber with the porosity of 1, which has the most obvious rectification and expansion effects.

Numerical Simulation

Distribution zone geometry.—To study the effect of various distribution zones using CFD, ten types of distribution zones were designed. The schematic of the ten investigated distribution zones is shown in Fig. 4. The area of the reaction zone is 250×80 mm^2, which consists of 40 parallel channels, equally spaced with 40 ridges of the same (1 mm) width. The depth of the gas channel is 0.5 mm.

Cases CRDZ 1–3 and CRDZ 4–6 were designed to investigate the effects of bifurcation number and turning angle, respectively. For CRDZ 1–3, the ratio of channel width to ridge width is set to be unity. Therefore, the area of the distribution zone decreases with an increase in m. Cases CRDZ 4–6 have the same bifurcation number. The geometry parameters of these cases are listed in Table II.

For the DMDZ design, the gas can flow across the entire distribution zone. The mass flow rate and pressure distribution are difficult to calculate analytically. Four types of distribution zones were designed with cylinder spacing 2, 3, and 4 mm and cylinder diameter 1 mm. The empty chamber distribution zone (hereafter termed as ECDZ) was designed for comparison. The corresponding porosities are 81.6%, 91.9%, 95.3% and 100% for the four cases of distribution zones, respectively.

Mathematic model.—Based on the assumptions in theoretical analysis section, the steady state Navier-Stokes equations for constant density and viscosity are solved for the single phase flow in the flow field:

Mass conservation equation:

$$\nabla \cdot (\vec{v}) = 0 \quad [15]$$

Momentum conservation equation:

$$\rho \vec{v} \cdot \nabla \vec{v} = -\nabla p + \mu \nabla^2 \vec{v} \quad [16]$$

It is noted that the flow is assumed to be laminar.

Boundary conditions and mesh independence.—The inlet boundary conditions were the mass flow inlet. The mass flow rate at the inlets was calculated at 200 and 1000 mA cm^{-2} with a stoichiometry of 2.0. The outlet boundary conditions were pressure out. The temperature was 348.15 K, and the relative humidity was 70%. All simulations were carried out using ANSYS Fluent software. The properties and parameters are listed in Table III. A grid independence test was performed to ensure that the results were independent of the number of mesh elements. The inlet average

Table II. Parameters for flow field models with CRDZ.

	a (mm)	b (mm)	α (°)	β_i (°)	γ_i (°)	m	n
CRDZ 1	40	40	45	90	90	2	20
CRDZ 2	20	20	45	90	90	4	10
CRDZ 3	10	10	45	90	90	8	5
CRDZ 4	40	40	0	β_{i0}	γ_{i0}	2	20
CRDZ 5	40	40	22.5	β_{i0}	γ_{i0}	2	20
CRDZ 6	40	40	45	β_{i0}	γ_{i0}	2	20

(a) 3.492×10^{-5} kg/s by theory

(b) 3.492×10^{-5} kg/s by CFD

(c) 1.746×10^{-4} kg/s by theory
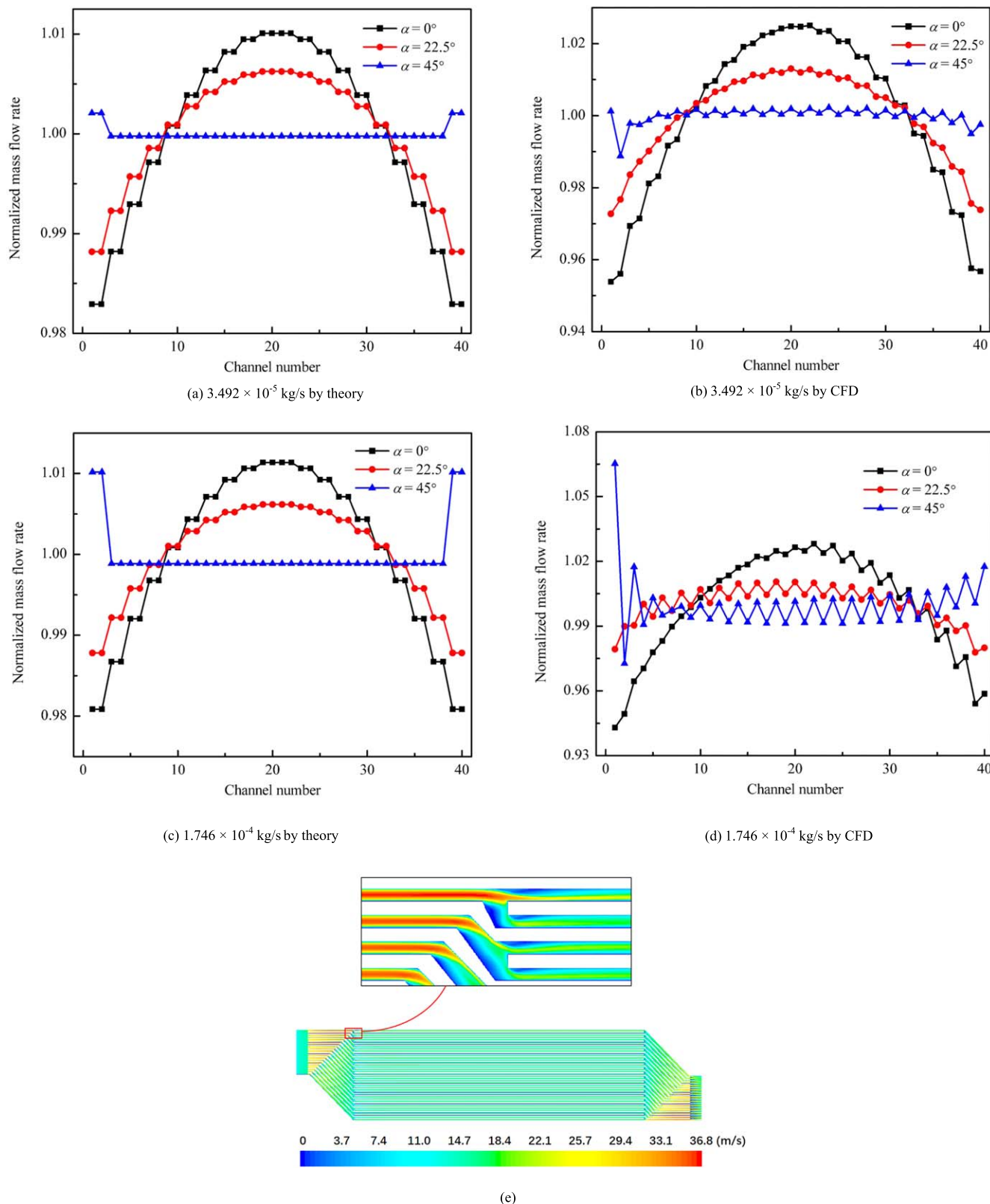

(d) 1.746×10^{-4} kg/s by CFD

(e)

Figure 8. (a–d) Normalized mass flow rate distributions in flow fields with CRDZ 4–6 at 3.492×10^{-5} kg s^{-1} and 1.746×10^{-4} kg s^{-1} obtained by theory and CFD. (e) Flow velocity distribution in Unit 1 of flow field with CRDZ 6 at 1.746×10^{-4} kg s^{-1}.

pressure represents the pressure drop of the flow field because of the pressure outlet setting. Figure 5a shows the inlet average pressure and mass flow rate in channel 1 of the flow field with CRDZ 1 at 1.746×10^{-4} kg s^{-1}. It can be seen that the average pressure and

mass flow rate did not exhibit any significant change for a mesh with more than 14 million elements whose grid structure is shown in Fig. 5b. Therefore, a mesh with 14 million elements was used for the rest of the simulation.
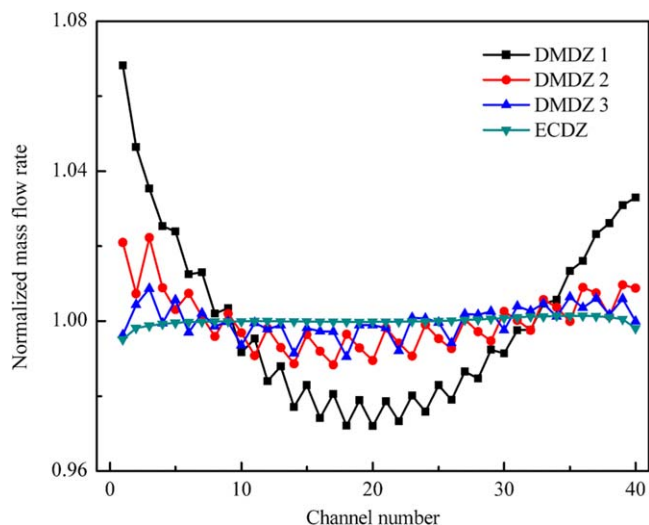
Figure 9. Normalized mass flow rate distributions in flow fields with DMDZ 1–3 and ECDZ at 1.746×10^{-4} kg s^{-1}.

Results and Discussion

Effects of channel-ridge distribution zone.— *Bifurcation number.*—Figure 6 shows the normalized mass flow rate distributions (the mass flow rate is divided by mean) and comparison of flow velocities of flow fields with CRDZ 1–3 at 1.746×10^{-4} kg s^{-1}. As mentioned in Section "**Channel-ridge distribution zone**", one channel in the distribution zone branches into m flow channels in the reaction zone, which make up a unit. As the dimension of the inlet becomes smaller, the m-value should increase to accommodate the fixed cell width. From Fig. 6a, one can see that the mass flow rate in each unit of each flow field is almost the same regardless of the

Table III. Properties and parameters.

Temperature (K)	348.15
Stoichiometry	2.0
Relative humidity (%)	70
Inlet mass flow rate (kg s^{-1})	$3.492 \times 10^{-5}/1.746 \times 10^{-4}$
Pressure at outlet (kPa)	101.3

m-value. However, the flow velocity is uneven in one unit due to the asymmetry of the structure, as shown in Fig. 6b. With an increase in the m-value, the mass flow rate distribution becomes non-uniform, e.g., the relative standard deviations (RSD) of mass flow rate in flow fields with CRDZ 1–3 are 3.2%, 13.1% and 29.6%, respectively. Because the flow velocity in the distribution zone becomes greater with higher m as indicated in Eq. 5, the unevenness in each unit is apparent.

Figure 7 shows a comparison of pressure drops of flow fields with CRDZ 1–3 computed by Eq. 12 and CFD simulation. Both methods show that pressure drop increases with the bifurcation number m. The predicted value with CFD is greater than that by theory, and the discrepancy increases with m. This discrepancy is primarily due to the assumption of evenly distributed gas in each unit for the theoretical method, which results into lower pressure drop.

Turning angle.—Flow fields with CRDZ 4–6 are designed to investigate the impact of turning angle α with $m = 2$. Figures 8a to 8d show their normalized mass flow rate distributions at 3.492×10^{-5} kg s^{-1} and 1.746×10^{-4} kg s^{-1} obtained by theory and CFD, respectively. The mass flow rate distribution becomes more uniform with an increase in α-value, and the distribution results obtained by CFD agree well with those obtained by theory. The reason for the phenomena is that the flow resistance in each channel tends to be equal when α increases to α_0. However, the mass flow rates in Units 1 and 20 are larger than those in the other units when α is equal to α_0, because
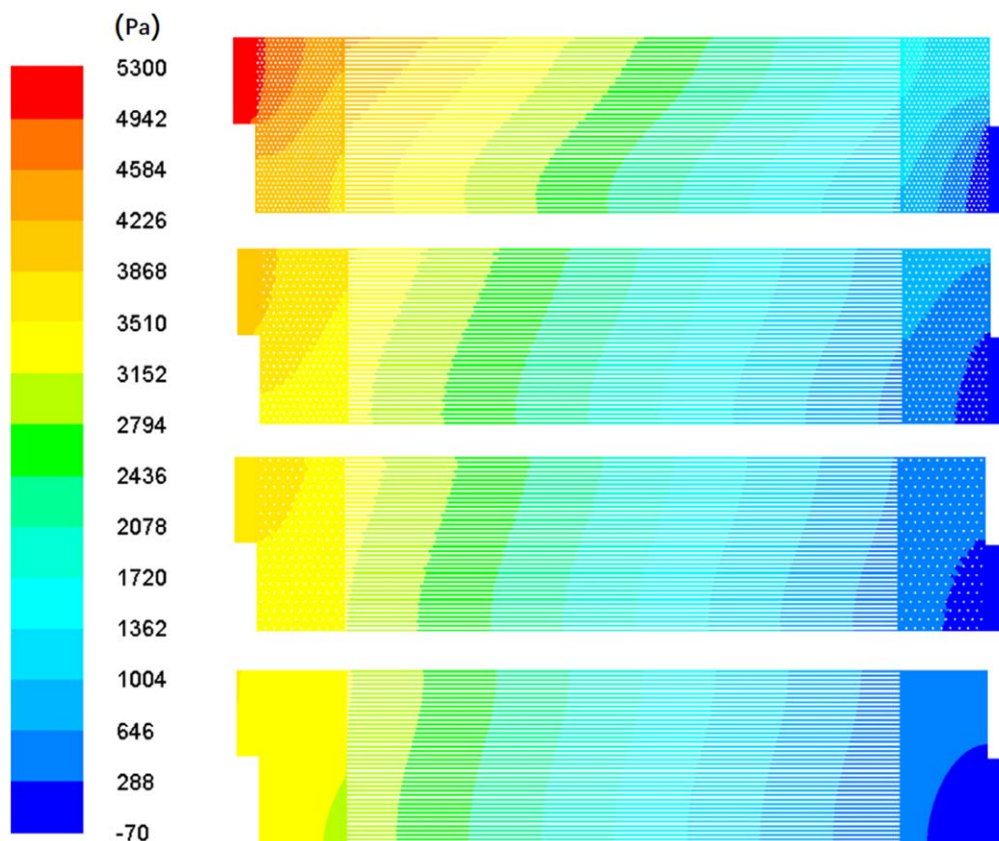

Figure 10. Pressure distributions in flow fields with DMDZ 1–3 and ECDZ at 1.746×10^{-4} kg s^{-1}.
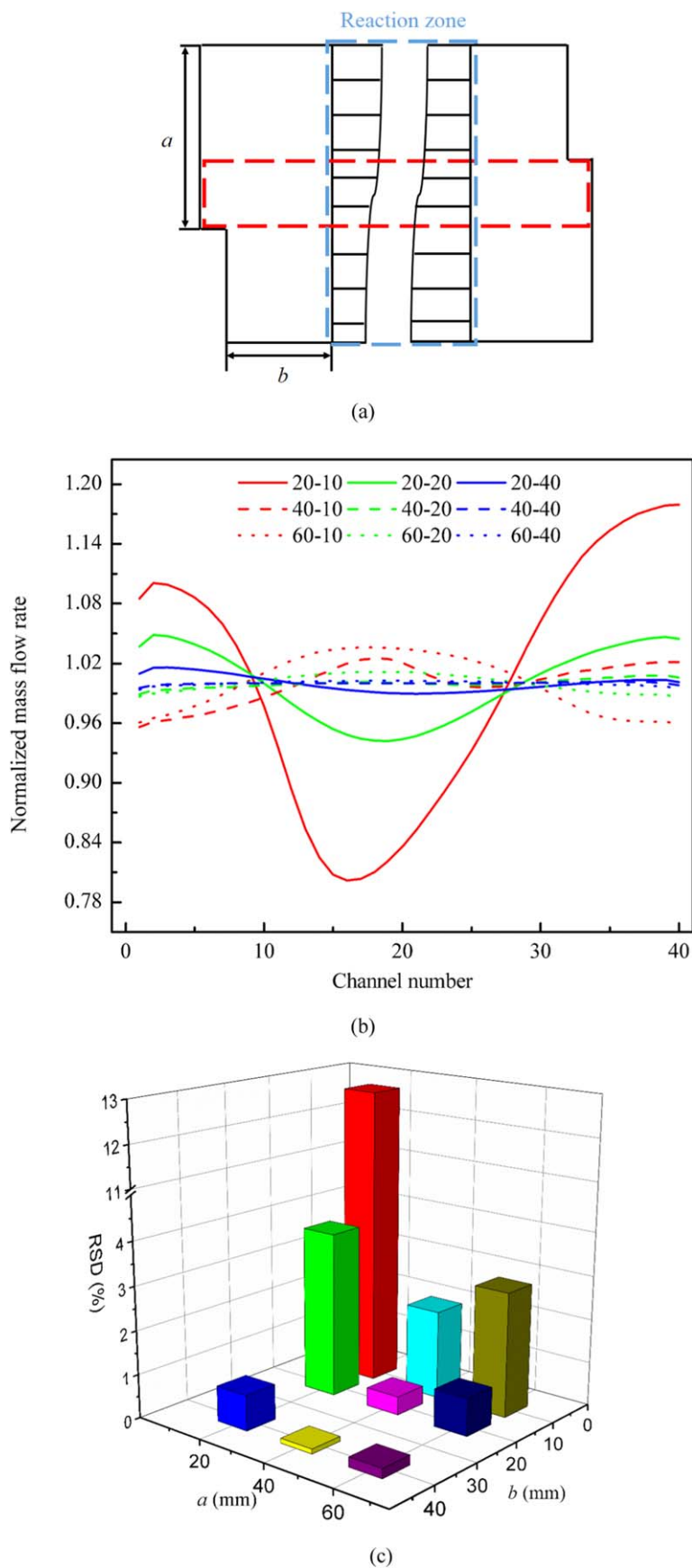
Figure 11. (a) Schematic of the flow fields with ECDZ. (b)Normalized mass flow rate distributions and (c) the RSD of mass flow rate in flow fields with various a- and b- values at 1.746×10^{-4} kg s^{-1}.

the local resistances in Units 1 and 20 are smaller than those in the other units due to less folds. A comparison of Figs. 8a–8d shows that the mass flow rates in Units 1 and 20 are more uneven when the total flow rate increases from 3.492×10^{-5} kg s^{-1} to 1.746×10^{-4} kg s^{-1}. This is because the effect of the local flow resistance on gas distribution accounts for a larger proportion when the flow velocity is larger.

According to the results obtained by CFD, the mass flow rates of the two channels in each unit, especially in Unit 1, are uneven. And the phenomenon is more obvious with the increase of gas flow rate. In theoretical analysis section, the gas is assumed to be evenly distributed when the channel in the distribution zone branches into two in the reaction zone, which results in the difference between the mass flow rate distributions obtained by theory and CFD. The gas distribution is uneven due to the asymmetry of the structure in actual flow fields, and it is more obvious in Unit 1 as shown in Figures 8e. Therefore, it is necessary to optimise the channel structures when designing an actual flow field by CFD, such as narrowing channel 1, to promote the distribution uniformity.

The pressure drops of flow fields with CRDZ 4–6 are 4.9, 5.1, 5.4 kPa obtained by theory and 4.9, 5.2, 5.4 kPa by CFD. The results agree well with each other. The pressure drops increase slightly with an increase in angle α, the effect of which on pressure drop can be ignored compared with bifurcation number m as described in Fig. 7.

Therefore, to design the flow fields with CRDZ, we can arrange the channels with simple geometry lines in the first step. Subsequently, the actual structure can be optimised with CFD considering the channel width, depth, etc. to achieve a more uniform distribution and suitable pressure drop.

Effects of dot matrix distribution zone.—Figure 9 shows the normalized mass flow rate distributions in flow fields with DMDZ 1–3 and ECDZ. With a decrease in the density of the dot matrix which causes an increase in porosity of distribution zone, the distribution uniformity in the reaction zone increases. When the distribution zone is an empty chamber, the distribution in the flow field is the most uniform. Figure 10 shows the pressure distributions in flow fields with DMDZ 1–3 and ECDZ. It can be seen that the pressure contour in the reaction zone tends to be vertical to the flow direction when the porosity of distribution zone increases. The rectification and expansion effects of distribution zone are more evident; thus, the flow rate distributions become more uniform. It is pointed out that the fluctuating distributions of flow rate in flow fields with DMDZ 1–3 are caused by the dots arrangement at the entrance of the reaction zone. The pressure drops of flow fields with DMDZ 1–3 and ECDZ are 5.2, 4.1, 3.8 and 3.5 kPa, respectively.

Table IV. Sizes of various ECDZs.

a/mm	20	20	20	40	40	40	60	60	60
b/mm	10	20	40	10	20	40	10	20	40

With an increase in porosity, the pressure drop decreases, which can be explained by Eq. 14.

With an increase in porosity, the shunt and dispersion effects of dot matrix are weaker; however, the rectification and expansion effects of the distribution zone are more obvious as mentioned in Section "**Dot matrix distribution zone**". This explains why the most uniform distribution and the lowest pressure drop occur when the porosity of distribution zone is 1.

Based on the above results, the distribution performance of the ECDZ is better than that of the DMDZ. To optimise the structure of ECDZ, a series of flow fields with various inlet widths and lengths of distribution zones were designed for further study. The schematic of the flow fields with ECDZ is shown in Fig. 11a. The parameters are listed in Table IV.

Figures 11b and 11c show the mass flow rate distributions and their relative standard deviations in flow fields with different a and b. The results indicate that the uniformity of the flow field first improves and then worsens with an increase in a-value as shown in Fig. 11b. This is because the flow velocity decreases with an increase in a, and the effects of expansion and rectification effects in ECDZ are better. However, when a increases by more than half of the width of the flow field, the mass flow rate at the channels, which are inside the red box as shown in Fig. 11a, becomes larger because the channels connect to the inlet and outlet of the flow field directly. The distribution is most uniform when a is 40 mm, which is half of the flow field width. The uniformity of the flow field improves with an increase in b-value, which enhances the effects of rectification in ECDZ. However, an increase in b is not required after the flow is fully developed because it will reduce the utilisation rate of the flow field.

Figure 12 shows the pressure distributions in ECDZ 20–10 and 60–40. The pressure in the borderline between the distribution and reaction zones is extremely uneven in ECDZ 20–10. However, it is almost the same in ECDZ 60–40. This demonstrates that a
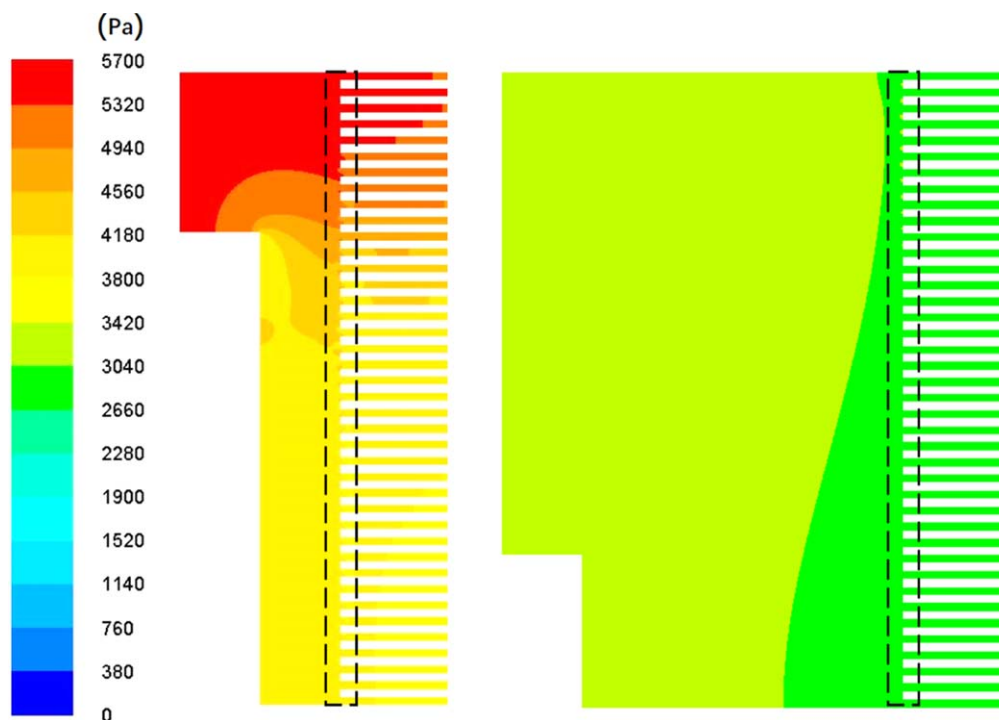

Figure 12. Pressure distributions in the borderline between distribution zone and reaction zone of flow fields with ECDZ 20–10 and 60–40 at 1.746×10^{-4} kg s^{-1}.

sufficiently large ECDZ can expand and rectify the gas flow and is beneficial to gas distribution.

In the present paper we focus mostly on only the effects of distribution zone design on flow uniformity and pressure drop. For DMDZ and ECDZ in real applications, there is a need to have sufficient number of dots to prevent area closure due to differential pressure. The dot matrix may have different arrangement, therefore, an optimal design must be carried out.

Conclusions

The impacts of two types of distribution zones, namely the channel-ridge and the dot matrix zones, on gas distribution uniformity and pressure drop were studied. First, the effects of the channel arrangement and dot arrangement in the distribution zone were analysed based on theoretical fluid dynamics and the theory of packed bed. Subsequently, a series of flow fields with different distribution zone designs was simulated using CFD. Some conclusions drawn from this study are as follows.

For the flow fields with CRDZ, the mass flow rates and pressure distributions obtained by theory and CFD agree well. The main difference is the uneven distribution within each unit when one channel in CRDZ bifurcates into more channels in the reaction zone. The mass flow rate distribution in the flow fields becomes more uniform when α increase to α_0 ($\alpha_0 = arctan(b/a)$), demonstrated by theory and CFD. Therefore, to design the flow fields with CRDZ, one can arrange the channels with simple geometry lines as the first estimate. Subsequently, the actual structure can be optimised with CFD considering the channel width, depth, etc. to achieve a more uniform distribution and suitable pressure drop.

For the flow fields with DMDZ, the uniformity of gas distribution depends on the shunt and dispersion effects of dot matrix, and the rectification and expansion effects of the distribution chamber. The uniformity in the reaction zone increases with increasing porosity of DMDZ. When the distribution zone is an empty chamber, the gas distribution in the flow field is the most uniform. For the flow fields with ECDZ investigated, when the width of the inlet is 40 mm i.e. half of the entire flow field, and the length of the distribution zone is longer than 20 mm, the distribution uniformity is quite good.

In this study, issues such as liquid water removal, assembly force, and sealing of the flow field plate were not considered. The actual flow field design with a distribution zone should be modified to address these issues accordingly. Further investigations are required to assess the impact of these factors.

Acknowledgments

ORCID

Yuan Yu https://orcid.org/0000-0002-0102-7358

References

1. Y. Wang, B. Seo, B. Wang, N. Zamel, and X. C. Adroher, *Energy AI*, **1**, 100014 (2020).
2. X. Li and I. Sabir, *Int. J. Hydrogen Energy*, **30**, 359 (2005).
3. X. D. Wang, X. X. Zhang, W. M. Yan, D. J. Lee, and A. Su, *Int. J. Hydrogen Energy*, **34**, 3823 (2009).
4. D. Spernjak, A. K. Prasad, and S. G. Advani, *J. Power Sources*, **195**, 3553 (2010).
5. J. Bachman, A. Santamaria, H. Y. Tang, and J. W. Park, *J. Power Sources*, **198**, 143 (2012).
6. D. H. Jeon, S. Greenway, S. Shimpalee, and J. W. V. Zee, *Int. J. Hydrogen Energy*, **33**, 1052 (2008).
7. A. D. Santamaria, N. J. Cooper, M. K. Becton, and J. W. Park, *Int. J. Hydrogen Energy*, **38**, 16253 (2013).
8. N. J. Cooper, A. D. Santamaria, M. K. Becton, and J. W. Park, *Energ. Convers. Manage.*, **136**, 307 (2017).
9. V. Ionescu, *J. Phys. Conf. Ser.*, **1297**, 012017 (2019).
10. W. Ming, K. He, P. Li, Y. Lei, and Y. Yong, *IOP Conf. Ser.: Mater. Sci. Eng.*, **274**, 012148 (2017).
11. W. M. Yan, H. Y. Li, and W. C. Tsai, *J. Electrochem. Soc.*, **153**, A1984 (2006).
12. G. M. Choi, D. S. Ko, J. S. Yang, D. J. Kim, J. H. Jeong, and Y. M. Kang, *J. Mech. Sci. Technol.*, **24**, 537 (2010).
13. S. Tong, J. C. Bachman, A. Santamaria, and J. W. Park, *J. of Power Sources*, **242**, 195 (2013).
14. N. Guo, M. C. Leu, and U. O. Koylu, *Fuel Cells*, **14**, 876 (2015).
15. F. Mojica, M. A. Rahman, J. M. Mora, J. D. Ocon, and P. A. Chuang, *Fuel Cells*, **20**, 547 (2020).
16. S. A. Atyabi and E. Afshari, *J. Therm. Anal. Calorim.*, **135**, 1823 (2018).
17. B. Timurkutluk and M. Z. Chowdhury, *Fuel Cells*, **18**, 441 (2018).
18. M. Z. Chowdhury and Y. E. Akansu, *Int. J. Hydrogen Energy*, **42**, 25686 (2017).
19. K. Kojima and K. Fukazawa, *ECS Trans.*, **69**, 213 (2015).
20. J. Kim, G. Luo, and C. Y. Wang, *J. of Power Sources*, **365**, 419 (2017).
21. G. Zhang, K. Jiao, and R. Wang, *Wcx World Congress Experience* (2018).
22. W. Li, Q. Zhang, C. Wang, X. Yan, S. Shen, G. Xia, F. Zhu, and J. Zhang, *Appl. Energy*, **195**, 278 (2017).
23. F. Mojica, M. A. Rahman, M. Sarker, D. S. Hussey, and P. A. Chuang, *Energ. Convers. Manage.*, **237**, 114095 (2021).
24. I. Mellor and A. Chapman, *8th Grove Fuel Cell Symposium* (2003), https://www.researchgate.net/publication/283329405_Development_of_BioMimetic_Flow-Field_Plates_for_PEM_Fuel_Cells.
25. J. P. Kloess, X. Wang, J. Liu, Z. Shi, and L. Guessous, *J. of Power Sources*, **188**, 132 (2009).
26. C. T. Wang, R. C. Hu, and R. L. Zheng, *Appl. Energy*, **87**, 1366 (2010).
27. K. Tüber, A. Oedegaard, M. Hermann, and C. Hebling, *J. of Power Sources*, **131**, 175 (2004).
28. D. Wen, L. Yin, Z. Piao, C. Lu, G. Li, and Q. leng, *Int. J. Heat Mass Transf.*, **121**, 775 (2018).
29. D. Wen, L. Yin, Z. Piao, C. Lu, G. Li, and Q. leng, *Int. J Energ. Res.*, **41**, 2184 (2017).
30. C. H. Chen, S. P. Jung, and S. C. Yen, *J. of Power Sources*, **173**, 249 (2007).
31. G. Su, D. Yang, Q. Xiao, H. Dai, and C. Zhang, *Renew. Energ.*, **173**, 498 (2021).
32. F. Barreras, A. Lozano, L. Valio, C. Marín, and A. Pa, *Scau, J. of Power Sources*, **144**, 54 (2005).
33. F. Barreras, A. Lozano, L. Valino, R. Mustata, and C. Mann, *J. of Power Sources*, **175**, 841 (2008).
34. Y. Cai, Z. Fang, B. Chen, T. Yang, and Z. Tu, *Energy*, **161**, 28 (2018).
35. Y. Liu, S. Bai, P. Wei, P. Pei, and H. Sun, *Energy Fuels*, **34**, 8857 (2020).
36. S. Shimpalee, S. Hirano, M. Debolt, V. Lilavivat, J. W. Weidner, and Y. Khunatorn, *J. Electrochem. Soc.*, **164**, E3073 (2017).
37. G. Zhang, X. Xie, B. Xie, Q. Du, and K. Jiao, *Int. J. Heat Mass Transf.*, **130**, 555 (2019).
38. M. Z. Chowdhury, O. Genc, and S. Toros, *Int. J. Hydrogen Energy*, **43**, 10798 (2018).
39. S. Haase, M. Moser, J. A. Hirschfeld, and K. Jozwiak, *J. of Power Sources*, **301**, 251 (2016).
40. H. Song, *Eng. Fluid Mech.* (Metallurgical Industry Press, Singapore) (2018).
41. J. Deng, Z. Lei, and L. Zhong, *J. Phys. Conf. Ser.*, **916**, 012023 (2017).
42. J. Jamain, J. Touboul, V. Rey, and K. Belibassakis, *J. Mar. Sci. Eng.*, **8**, 960 (2020).
43. S. Ergun, *J. Mater. Sci. Chem. Eng.*, **48**, 89 (1952).